Materials Characterization 171 (2021) 110800

Contents lists available at ScienceDirect

Materials Characterization

journal homepage: www.elsevier.com/locate/matchar

The effect of major constituents on microstructure and mechanical properties of cast Al-Li-Cu-Zr alloy

Liang Wu [a,b], Xianfeng Li [a,*], Haowei Wang [a,b]

[a] State Key Laboratory of Metal Matrix Composites, Shanghai Jiao Tong University, No. 800 Dongchuan Road, Shanghai 200240, PR China
[b] School of Materials Science and Engineering, Shanghai Jiao Tong University, No. 800 Dongchuan Road, Shanghai 200240, PR China

ARTICLE INFO

Keywords:
Cast Al-Li-Cu alloys
Compositions
Microstructural evolution
Mechanical properties
Transmission electron microscopy

ABSTRACT

The effect of major constituents (the Li content increases from 0.5 to 3 wt% and the Cu content decreases from 4.5 to 2 wt%) on microstructure and mechanical properties of cast Al-Li-Cu-Zr alloy were studied to understand a qualitative assessment of sequence and kinetics of multiple precipitations. Increasing the Li content progressively raises the melting temperature from 520 °C in 1# alloy (Al-0.5Li-4.5Cu, wt%) and 2# alloy (Al-1Li-4.5Cu) to 560 °C in 6# alloy (Al-3Li-2Cu). In addition, the variations of the major constituents result in the changes of the type and volume fraction of the inter- and intra-granular intermetallic phases. TEM results indicate that minor modifications to alloy composition greatly alter precipitation behavior during isothermal aging. The Li-poor alloy (2# alloy) presents a much shorter incubation time of T_1-Al_2CuLi precipitate than the Li-rich alloy (Al-1.5Li-4.5Cu, 3# alloy), while the nucleation of θ'-Al_2Cu precipitate is promoted in Li-rich alloy. No typical spherical δ'-Al_3Li precipitate is observed in 2# and 3# alloys during isothermal aging, except for the as-quenched 3# alloy. The preferential nucleation of δ' precipitate on the coherent and broad face of θ' precipitate is observed in 2# and 3# alloys, leading to the formation of "sandwich-like" δ'/θ'/δ' phases. Further decreasing Cu content to 2 wt% and increasing Li content to 3 wt% (6# alloy), the predominant phase in the matrix is δ' precipitate, accompanied by a small amount of unevenly distributed θ' and T_1 precipitates. The best balance between ductility and strength is obtained by 2# alloy aged for 32 h, but 6# alloy has significant advantages in terms of density (2.437 g/cm^3) and elastic modulus (82.65 GPa) over 2# alloy (density: 2.675 g/cm^3; elastic modulus: 75.45 GPa).

1. Introduction

Age-hardening alloys based on the Al-Li system are of great interest for aircraft structural applications due to their outstanding combination of high elastic modulus, low density and high strength [1–3]. The addition of every one wt% of Li to Al alloys decreases the density of the alloy by ~3% but increases the elastic modulus by ~6% [4]. Therefore, lithium provides the most considerable reduction in density and the largest increase in elastic modulus of any known alloying element for aluminum alloys [5]. In Al-Li binary alloys, the solubility of Li in Al is up to ~4.2 wt%, and the strengthening of the alloy is mainly attributed to the formation of the ordered $L1_2$-Al_3Li (δ') precipitates [6,7]. Although the addition of Li element increases the strength significantly, the industrial application of binary alloy has restricted due to its low ductility and fracture toughness [8]. This drawback is originated from the shear localization in the matrix resulting from the planar slip associated with the shearable nature of the ordered δ' precipitate. Moreover, the presence of grain boundary precipitate and the precipitate free zone (PFZ) promotes the shear localization within a soft matrix at PFZ.

The coprecipitation of multiple hardening phases by adding the third alloying element, especially the Cu element, prevents the shear localization of binary Al-Li alloy, and its strengthening potential would become outstanding as a result of the complex combination of precipitates that form during heat treatment [9–11]. It is well known that the precipitation sequence mainly depends on the contents of the major constituents in the ternary Al-Li-Cu system, and many ternary precipitates would be formed during isothermal aging, among which, T_1-Al_2CuLi is the most significant one [12]. Moreover, according to alloy chemistry and thermomechanical processes, other minor precipitates, such as T_B-Al_7Cu_4Li and T_2-Al_6CuLi_3, can be formed, particularly at the grain boundary [13]. The multiple precipitation behavior in an alloy makes it difficult to understand the sequence of precipitation behavior

* Corresponding author.
E-mail address: brucelee75cn@sjtu.edu.cn (X. Li).

https://doi.org/10.1016/j.matchar.2020.110800
Received 15 July 2020; Received in revised form 17 November 2020; Accepted 29 November 2020
Available online 2 December 2020

precisely and requires more research on the precipitation behavior according to the composition. A few earlier researches had been done to study the effect of composition and thermomechanical process on comprehensive performance and microstructural evolution of deformed Al-Li-Cu alloys [14–16]; however, the range of alloy composition concerned is still very limited at present, with Li content changing from 0.7 to 1.5 wt% and Cu is around 3 wt%. The present study expands the alloy composition up to 3 wt% Li and 4.5 wt% Cu. More importantly, few literatures are available on the design of alloy chemistry, mechanical performance and microstructure characteristics of cast Al-Li-Cu alloy. This work is devoted to the development of cast Al-Li-Cu alloy, due to casting cannot only effectively alleviate the anisotropy of mechanical properties, but also provides a cost-effective approach to manufacture component of complex shapes. Most importantly, it is possible to study the effect of the major constituents varying in a wide range on the precipitation sequence and mechanical properties of the alloys due to the upper limit of the content of Li in cast Al-Li-Cu alloys could be much higher than that in deformed alloys. For better understanding the relevance between the compositions and properties of the Al-Li-Cu alloy and provide a guidance for subsequent research, it is, therefore, necessary to study the complex microstructure of these alloys with different compositions and the corresponding properties.

The present work aims at examining the effect of the major constituents on the precipitation behavior and mechanical properties of cast Al-Li-Cu alloys. In particular, this work focus on elucidating the successive microstructure evolution from as-quenched state to over-aged state, and to acquire a qualitative assessment of sequence and kinetics of precipitation.

2. Materials and methods

Six alloys were produced by the conventional casting method and the details of the melting procedures are available in our previous report [17]. The compositions of six alloys are listed in Table 1 and they are hereafter denoted as 1# - 6# alloys, respectively. In addition, 0.2 wt% Zr was added to all alloys to refine the grain and introduce the metastable, coherent β'-Al_3Zr phase, and the specific roles of β' phases have been detailed elsewhere [18]. The standard Archimedes method was used to determine the density of the alloys. An ET-RT modulus tester (JE2-C1, Nihon Techno-Plus, Japan) was used to determine the elastic modulus of each alloy with dimension of Φ 6 × 60 mm^3 according to the GB/T 22315–2008 standard [19]. The averaged results of density and elastic modulus are also shown in Table 1. The proper solution parameters were determined by the differential scanning calorimetry (DSC, 204F1) apparatus. The as-cast specimens were heat treated by a two-step solution treatment, followed by isothermal aging at 175 °C in an oil bath. Each step was terminated by water-quenching. Vickers microhardness was determined using mechanically polished samples (to a 0.02 μm finish) by a CARAT 930 Automatic Vickers microhardness testing machine with a load of 10 kg and a dwell time of 15 s. Metallographic specimens were mechanical polished and then etched with Keller's reagent for 15 s before observation. An Ultima IV X-ray diffractometer (XRD) was applied to identify the phase constitutions of as-cast alloys. Scanning Electron Microscope (SEM, TESCAN MAIA3 model 2016) and Optical microscope (OM, Zeiss Imager A1m) were used to observe the microstructure. Tensile tests of sheet specimens were conducted on Zwick/Roell universal testing machine with a strain rate of $1 \times 10^{-4}\ s^{-1}$. Selected samples were examined by transmission electron microscopy (TEM) using a JEOL 2100 microscope. Thin foils of the alloy samples were obtained by mechanical polishing and final electro-polishing, using a mixed solution of 25% nitric acid and 75% methanol at −35 °C and 30 V.

Table 1
Chemical compositions, density, and elastic modulus of six alloys.

Alloys	wt%	Density (g/cm^3)	Elastic modulus (GPa)
1#	Al-0.5Li-4.5Cu	2.729	71.73
2#	Al-1Li-4.5Cu	2.675	75.45
3#	Al-1.5Li-4.5Cu	2.622	78.32
4#	Al-2Li-4.5Cu	2.571	79.97
5#	Al-2Li-3Cu	2.546	79.34
6#	Al-3Li-2Cu	2.437	82.65

3. Results and discussion

3.1. Phase analysis and as-cast microstructure

Fig. 1 displays the phase constitutions of as-cast six alloys. Based on the patterns, the microstructure primarily consisted of θ-Al_2Cu phase and α-Al matrix in as-cast 1# alloy, while additional diffraction peaks from T_1-Al_2CuLi, T_2-Al_6CuLi_3, and T_B-$Al_{7.5}Cu_4Li$ phases are also identified well with the increase of Li content (2# and 3#). Further increasing Li content to 2 wt%, T_1 and T_2 phases are the dominant phases in 4# alloy, accompanied by a small amount of δ'-Al_3Li phase. As reported that when Li content in aluminum matrix exceeds a certain value, δ' phase would precipitate from the supersaturated solid solution during solidification, and its size, number density and volume fraction depend on the composition and cooling rate of the alloy [10,20]. Here it is noteworthy, that the intensity of diffraction peaks arisen from T_1 and T_2 phases in 4# alloy is the highest among six alloys, indicating the amount of T_1 and T_2 phases in 4# alloy is much higher. According to the XRD patterns, the phase constitution of 5# and 6# alloys are similar, and both are mainly composed of δ' and T_1 phases, which is consistent with previous investigation [21]. In addition, the diffraction peaks related to δ-AlLi phase are also found in 5# and 6# alloys. It is well known that the formation of θ, T_2, and δ phases is produced by the non-equilibrium solidification process, and the absence of the diffraction peaks associated with some other phases in the patterns may be owing to their low contents.

The optical microstructures of as-cast six alloys are shown in Fig. 2. The as-cast microstructures of all the six alloys are similar, and the matrix consisted of coarse intermetallic phases in the inter-dendritic region or at the grain boundary and typical dendritic α-Al grains. By carefully examining the as-cast metallographic structures of the six alloys, the following results can be obtained: (1) Comparing the optical microstructures of 1# to 4# alloys, the volume fraction of intermetallic phases at the grain boundary increases with the increase of Li content at the same Cu content, which matches well with the XRD results. Furthermore, the grain structure is refined gradually as the content of Li increases from 0.5 to 2 wt%, which is mainly owing to the enrichment of solute at the solid/liquid interface during solidification, i.e. constitutional undercooling [22]; (2) Comparing the optical microstructures of

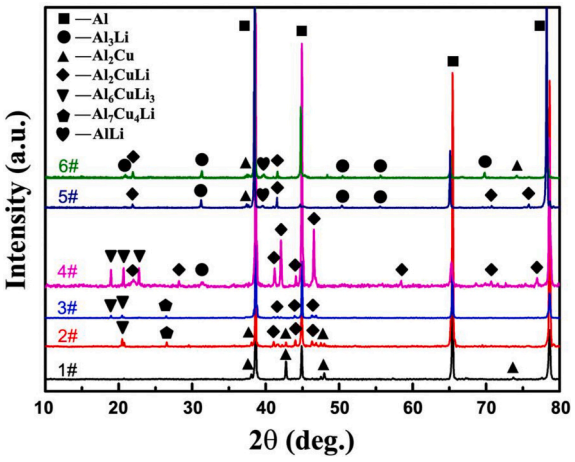

Fig. 1. XRD results of as-cast alloys with different compositions.

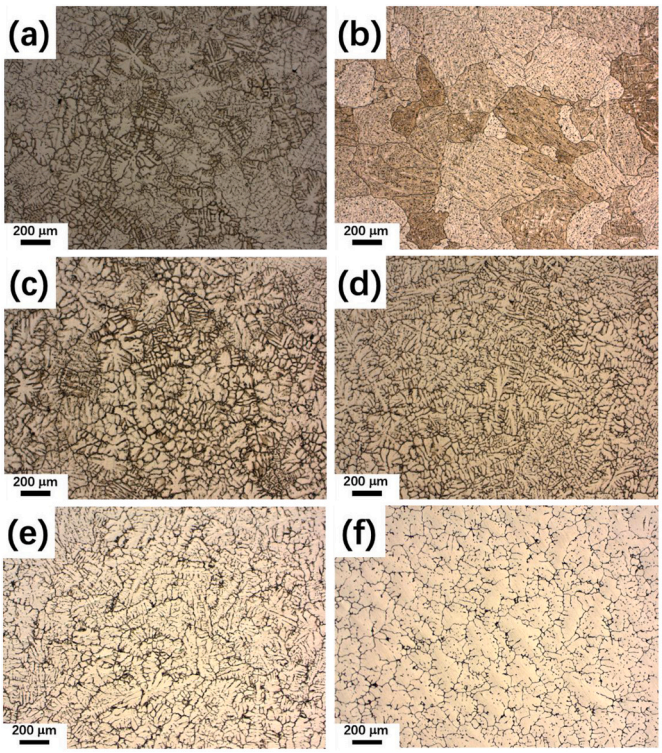

Fig. 2. The microstructures of as-cast alloys: (a) to (f) represent 1# to 6# alloys respectively.

4# and 5# alloys, the volume fraction of coarse intermetallic phases decreases with the decrease of Cu content at the same Li content; (3) Further increasing Li content to 3 wt% and decreasing Cu content to 2 wt % (6# alloy), the volume fraction of intermetallic phases is the lowest among the six alloys. This may due to the fact that the diffusion coefficient and the solute partition coefficient of Li in the Al matrix are much higher than that of Cu. As a result, Li atoms are more likely to remain in the matrix to form a solid solution during solidification, which reduces the tendency of the segregation of solute atoms at the grain boundary and decreases the volume fraction of coarse intermetallic phases [23].

Fig. 3 displays the un-etched SEM micrograph of as-cast 6# alloy and the corresponding distribution of Cu element acquired by EDS. Note that similar results of the other five alloys are not given here anymore. Coarse intermetallic phases with continuous networks morphology can be clearly observed (Fig. 3a). The distribution of Cu element is highly coincident with that of intermetallic phases, as shown in Fig. 3b, which is distributed along the grain boundary. However, these Cu-containing intermetallic phases, such as θ, T_2, and T_1, have not been identified since Li element cannot be detected by EDS.

3.2. Solution parameters and as-quenched properties

As shown in Fig. 2 and Fig. 3, there are a large number of coarse intermetallic phases at the grain boundary in the as-cast matrix. These coarse intermetallic phases are harmful to the ductility of the alloy, it is, therefore, necessary to dissolve these phases through proper heat treatment to eliminate their adverse effects. At the same time, through rapid-cooling methods such as quenching, numerous solute atoms would be retained in the matrix to form a supersaturated solid solution, which lays a good foundation for subsequent age-hardening. In order to select appropriate heat treatment parameters of the alloys with different compositions, six alloys were tested by DSC. Fig. 4 shows the high-temperature range (450–700 °C) of the DSC curves of the alloys. A distinct initial melting peak, which is attributed to the dissolution of Cu-containing intermetallic phases, can be clearly observed in all as-cast alloys, and the position of the initial melting peak of the alloys is different. This variation indicates that the types and volume fraction of intermetallic phase in the as-cast microstructure of six alloys are different, which is consistent with the XRD results. In order to dissolve intermetallic phase as much as possible and avoid the incipient melting, a two-step solution treatment was selected to allow the gradient dissolution of intermetallic phases. Based on the existence of several Cu-containing intermetallic phases with relatively low melting points in the as-cast matrix, the homogenization temperature commonly used in the cast Al-Cu alloys, 500 °C, is determined as the safe temperature of the first step [24], which, however, is insufficient to completely dissolve all the Cu-containing intermetallic phases according to the DSC results. Therefore, a relatively higher temperature for the second step (520–560 °C) is selected to further decrease the amount of these intermetallic phases and improve the supersaturated solid solubility of solute

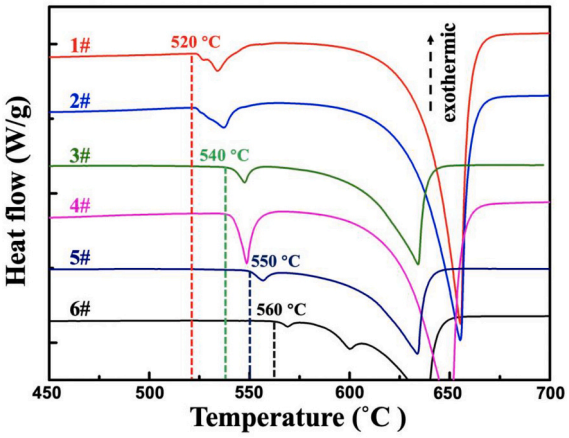

Fig. 4. DSC curves of the as-cast alloys.

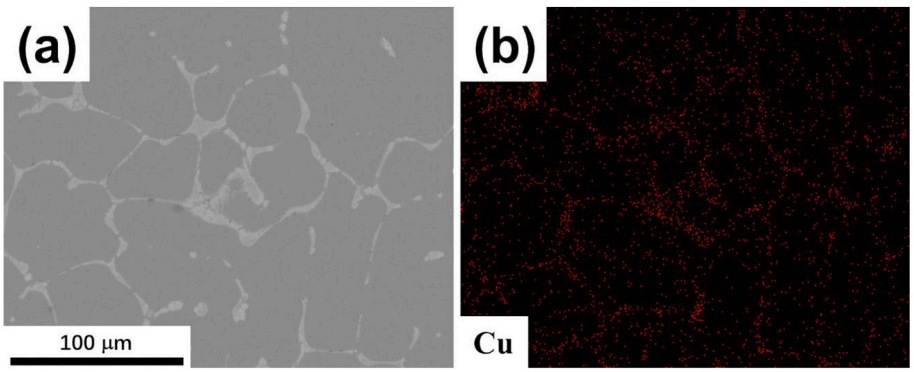

Fig. 3. (a) SEM micrograph of as-cast 6# alloy and (b) the corresponding distribution of Cu element.

atoms. Combining the practical metallographic observations with the results of DSC, the respective two-step heat treatment parameters for the six alloys are determined, as listed in Table 2.

The typical microstructures of the as-quenched alloys are shown in Fig. 5. In as-quenched samples, the bulk of intermetallic phases at the grain boundary are completely dissolved, except for 4# alloy. Some residual intermetallic phases are observed along the grain boundary in the as-quenched 4# alloy (Fig. 5d), which indicates that the second-step temperature, 540 °C, is also insufficient to completely dissolve all the intermetallic phases. The application of a higher temperature (560 °C), however, results in a typical incipient melting feature in 4# alloy, as illustrated in Fig. 6b. Even so, a large amount of residual intermetallic phases is still observed in the sample treated at 560 °C, as shown in Fig. 6a. Undoubtedly, these residual intermetallic phases will greatly damage the mechanical properties, hence the content of Li in cast Al-4.5Cu alloy (wt%) should not exceed 1.5 wt%.

Fig. 7a and b display the tensile test results, including ultimate tensile strength (UTS), yield strength (YS) and elongation (EL), and the corresponding engineering stress-strain curves of six alloys after solution treatment. YS of the alloys increases from 107 MPa to 130 MPa with increasing Li content at the same Cu content (4.5 wt%). While UTS firstly increases as Li content increases from 0.5 to 1.5 wt%, and then decreases. The highest UTS obtained by 3# alloy is 321 MPa. As anticipated, EL decreases with increasing Li content, especially of 4# alloy. This sharp reduction of EL of 4# alloy is mainly ascribed to the undesirable residual intermetallic phases in the as-quenched state. Moreover, the addition of Li element can improve the work hardening rate of the alloys, which is confirmed by the stress-strain curves of 1# to 3# alloys in Fig. 7b. The higher work hardening rate leads to a larger yield ratio of 2# and 3# alloys with lower EL, than 1# alloy. Note that the lowest YS and UTS obtained by 5# alloy is 93.3 MPa and 258 MPa, respectively. In addition, YS and EL of 6# alloy are close to those of 3# alloy, while UTS is slightly lower than the latter. Therefore, 3# and 6# alloys are considered to have superior comprehensive performance.

It is worth mentioning that Table 1 also lists the density and elastic modulus of the alloys studied in this work. As shown in Table 1, the density gradually decreases from 2.729 g/cm^3 of 1# alloy to 2.437 g/cm^3 of 6# alloy with the increase of Li content and the decrease of Cu content, while the elastic modulus gradually increases from 71.73 GPa of 1# alloy to 82.65 GPa of 6# alloy. Therefore, compared with other conventional cast aluminum alloys (density: 2.7–2.8 g/cm^3; elastic modulus: 70 GPa), cast Al-Li-Cu alloys, especially those with high Li content, have significant advantages in terms of density and elastic modulus. In addition, Fig. 7c displays the specific properties involving specific modulus (Elastic modulus / Density, E/ρ), specific YS (Yield strength / Density, $\sigma_{0.2}/\rho$) and specific UTS (Ultimate tensile strength / Density, σ_b/ρ) of the six alloys after solution treatment. It can be clearly seen that the specific modulus is determined by the Li content, and its value increases with the increase of Li content and gradually increases from 0.26×10^8 m^2/s^2 of 1# alloy to 0.34×10^8 m^2/s^2 of 6# alloy. The specific YS and specific UTS are determined by both density and strength which is not only determined by Li content, but also affected by Cu content, and the change trend of the specific YS and specific UTS is the same. From 1# alloy to 6# alloy, their values increase first and then decrease, and finally reach the maximum value at 6# alloy. It can be deduced from Fig. 7 that, in as-quenched state, 6# alloy not only has excellent mechanical properties, but also has significant advantages in density, modulus and specific properties.

Table 2
Solution treatment parameters of the six alloys.

Alloys	wt%	Solution parameters
1#	Al-0.5Li-4.5Cu	500 °C × 32 h + 520 °C × 24 h
2#	Al-1Li-4.5Cu	500 °C × 32 h + 520 °C × 24 h
3#	Al-1.5Li-4.5Cu	500 °C × 32 h + 540 °C × 24 h
4#	Al-2Li-4.5Cu	500 °C × 32 h + 540 °C × 24 h
5#	Al-2Li-3Cu	500 °C × 32 h + 550 °C × 24 h
6#	Al-3Li-2Cu	500 °C × 32 h + 560 °C × 24 h

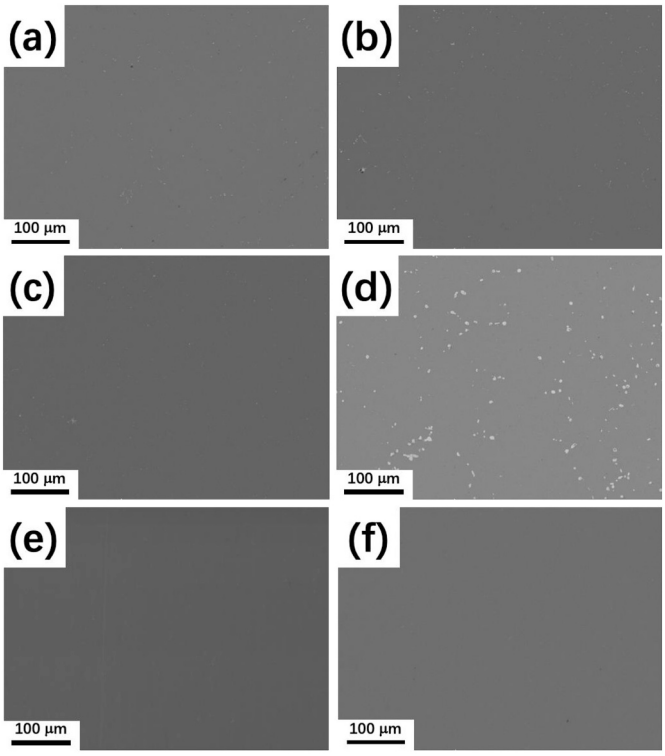

Fig. 5. SEM micrographs of the as-quenched alloys: (a) to (f) represent 1# to 6# alloys respectively.

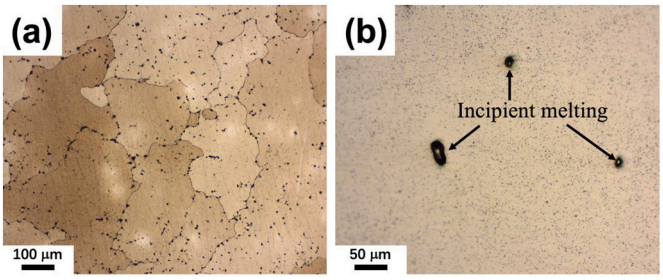

Fig. 6. (a) Optical microstructures of 4# alloy solution treated at 500 °C × 36 h + 560 °C × 24 h; (b) the enlarged image, indicating that the occurrence of incipient melting.

Comprehensively considering the tensile test results in as-quenched state, density, elastic modulus and specific properties of the six alloys, we selected three representative alloys (2#, 3# and 6#) for further characterization in order to investigate the effect of variations in the major constituents on precipitation behavior.

3.3. Precipitation kinetics and sequence

Fig. 8a displays the evolution of microhardness of 2#, 3#, and 6# alloys during isothermal aging. In as-quenched state, the microhardness values of 2# and 6# alloys are similar and are slightly lower than that of 3#. By carefully examining the microhardness evolution of the three alloys, the following results can be obtained: (1) a similar and noteworthy softening behavior occurs in 2# and 3# alloys in the initial stage of aging, attributing to some of the microstructural features (GP zones or solute clusters formed during natural aging) are dissolved or revised by

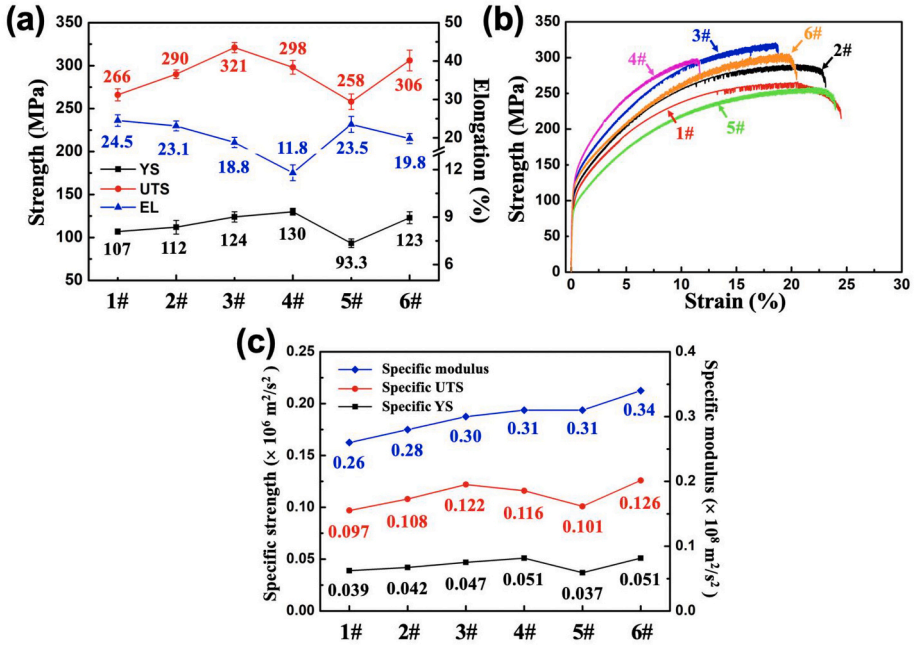

Fig. 7. (a) Mechanical properties, (b) representative engineering stress-strain curves and (c) specific properties of the six alloys after solution treatment.

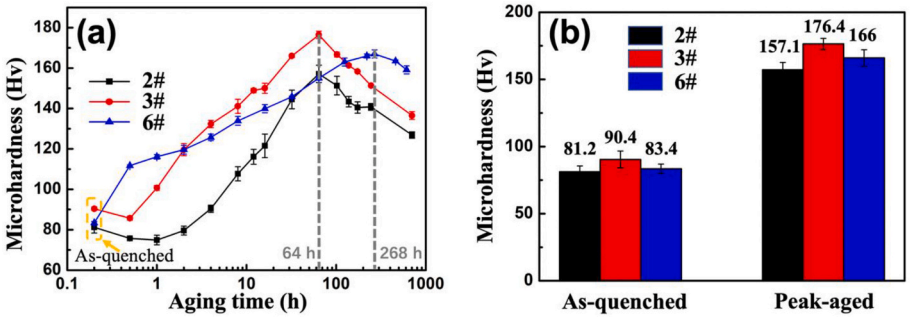

Fig. 8. (a) Vickers microhardness evolution of three alloys during isothermal aging at 175 °C; (b) the microhardness comparison between as-quenched and peak-aged states.

the rise in temperature [14]; (2) The duration and amplitude of the softening behavior of 2# alloy are greater than those of 3# alloy, indicating that Li content may affect the formation of clusters in the matrix. Kumar et al. [25] studied the effect of lithium concentration on the precipitation behavior of aluminum-lithium alloy. The results suggested that moderate Li atoms in solid solution could promote the formation of clusters, but when the Li content exceeds the critical value, the δ' phase formed in the matrix would hinder the formation of clusters; (3) After the end of softening, a steep increase in microhardness is clearly observed to happen in 2# and 3# alloys, and then the microhardness reaches its maximum value at 64 h. Subsequently, both alloys enter an over-aged state, and the microhardness decreases significantly; (4) The initial aging response of 6# alloy is extremely fast, but then the microhardness increases at a slower rate than the other two alloys, resulting in a significant extension of the time required for the peak-aged state. It should be note that all the three alloys possess a strong aging-hardening, and the microhardness increments of the three alloys during isothermal aging are approximately the same (see Fig. 8b). The highest peak-microhardness is obtained in 3# alloy (176.4 HV), followed by 6# alloy and 2# alloy.

In order to better explain the relationship between the evolution of microhardness and microstructure, the samples of the alloys in various aging states, including 0 h (as-quenched, AQ), 8 and 32 h (under-aged, UA), 64/268 h (peak-aged, PA), and 256/600 h (over-aged, OA), were examined by TEM in detail. It should be noted that because the aging responses of the three alloys are quite different, the time nodes selected in peak-aged and over-aged states are also different. Note that unless otherwise specified, dark-field micrographs are obtained from superlattice reflections of δ' phase.

Before aging, no precipitate is observed in 2# alloy, which can also be confirmed by SAD pattern shown in Fig. 9b. In terms of 3# and 6# alloys, the heterogeneous dispersion of β'-Al_3Zr particles (formed during heat treatment) and the homogeneous distribution of fine δ'-Al_3Li precipitates are clearly observed, as illustrated in Fig. 9c - f. The $L1_2$ superlattice reflections from δ' precipitates can also be clearly identified in the corresponding diffraction patterns. In addition, the size and volume fraction of δ' precipitate in 6# alloy are significantly larger than those in 3# alloy, indicating that the increase of Li concentration promotes the precipitation of δ' phase. It has been suggested that precipitation behavior of Al-Li alloy in the initial stage of aging is mainly determined by Li content, and the homogeneous distribution of fine δ' precipitate can always be observed in the as-quenched sample containing more than 2 wt% Li [20]. Obviously, the result of this work is inconsistent with the earlier report on the initial precipitation kinetics of δ'. In this work, the content of Li in 3# alloy is 1.5 wt%, which is lower than the critical value reported in the literature, but many fine δ'

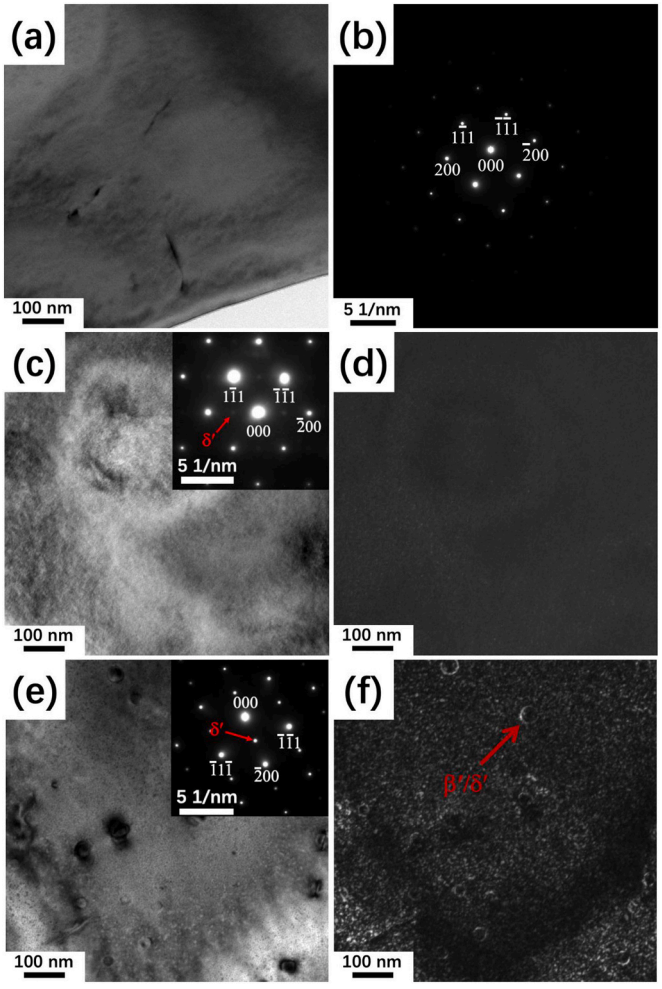

Fig. 9. TEM micrographs of the three alloys after solution treatment: (a) BF micrograph of 2# alloy; (b) the corresponding SAD pattern viewed along $[011]_{Al}$ zone axis; (c) BF micrograph and SAD pattern viewed along $[011]_{Al}$ zone axis of 3# alloy; (d) the corresponding DF micrograph of 3# alloy; (e) BF micrograph and SAD pattern viewed along $[011]_{Al}$ zone axis of 6# alloy; (f) the corresponding DF micrograph of 6# alloy.

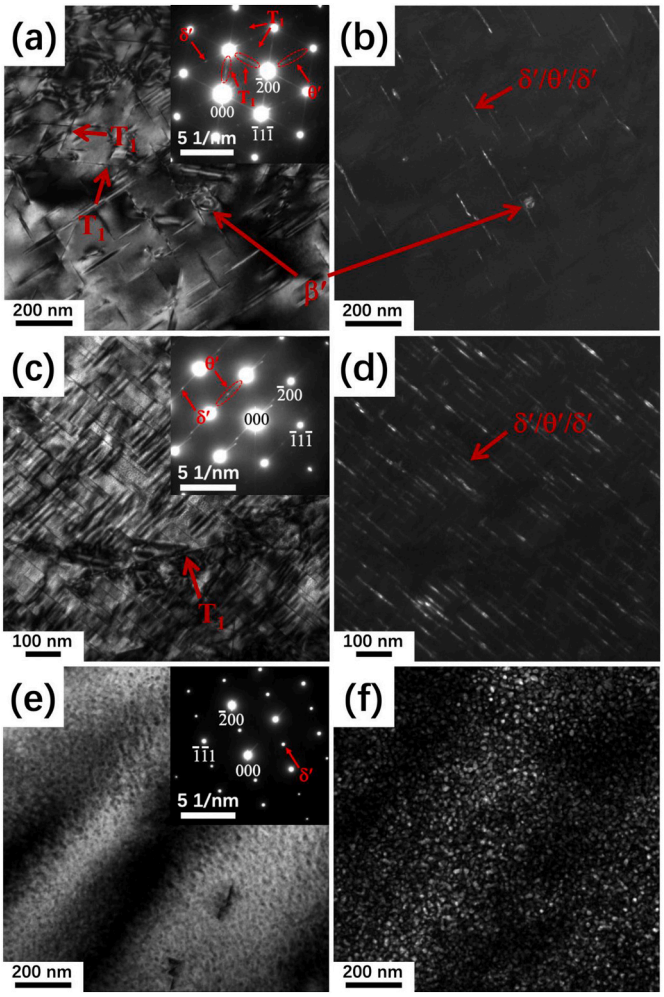

Fig. 10. TEM micrographs of the three alloys in UA state (8 h): (a) BF micrograph and SAD pattern viewed along $[011]_{Al}$ zone axis of 2# alloy; (b) the corresponding DF micrograph of 2# alloy; (c) BF micrograph and SAD pattern viewed along $[011]_{Al}$ zone axis of 3# alloy; (d) the corresponding DF micrograph of 3# alloy; (e) BF micrograph of grain interior and grain boundary of 6# alloy; (f) the corresponding DF micrograph and SAD pattern viewed along $[011]_{Al}$ zone axis of 6# alloy.

precipitates are also observed in the as-quenched state. This difference may due to the presence of Cu element and different solution temperature and cooling rate of the alloys. The congruent ordering prior to decomposition into δ' precipitate and the solid solution could provide a plausible explanation for the rapid formation of δ' precipitates in the as-quenched state [26]. Moreover, the typical core-shell β'/δ' dispersoids are also observed in the matrix (Fig. 9f), which is due to the heterogeneous nucleation of δ' on pre-existing β' dispersoids. The β'/α-Al heterophases interface was identified as the preferential nucleation site for δ' phase as a result of the decrease of both strain and surface energies [27,28].

The bright-field (BF) and δ'-centered dark-field (δ'-CDF) micrographs of the three alloys in UA state (8 h) are shown in Fig. 10. Obviously, some new precipitates are introduced in 2# and 3# alloys after aging. Note that, other strengthening precipitates, such as θ'-Al_2Cu and T_1-Al_2CuLi phases, can be distinguished according to their respective orientation relationships with the matrix, and the detailed descriptions of these precipitates also can be found in our previous work [6]. As shown in Fig. 10a, a large number of fine T_1 and θ' precipitates are found in BF micrograph of 2# alloy. The presence of θ' and T_1 precipitates is also confirmed by the SAD pattern inset in Fig. 10a [29]. Interestingly, the $L1_2$ superlattice spots arisen from δ' precipitate in the diffraction patterns of 2# and 3# alloys are prominent, but no typical spherical δ' precipitate is found in the DF micrographs. Although an isolated $L1_2$-β' particle is observed in 2# alloy, one $L1_2$-β' particle is insufficient to cause such significant superlattice spots. Therefore, as marked in Fig. 10b, δ' precipitates in 2# and 3# alloys are considered to nucleate preferentially on the broad and coherent interface between the matrix and θ' precipitates, leading to the formation of "sandwich-like" δ'/θ'/δ' phases [30]. In addition, some θ' precipitates formed around the β' dispersoid are also found (Fig. 10b), providing support for the report of C. Yang et al. [31]. The authors proposed that the heterogeneous nucleation of θ' precipitate on β' dispersoids was primarily ascribed to the reduction of interfacial energy. The most striking feature of the microstructure of 3# alloy is the dissolution of fine spherical δ' precipitates existing in the as-quenched matrix, which is consistent with the softening behavior of the alloy during the initial aging. This indicates that the fine spherical δ' precipitates existing in the as-quenched state is unstable due to its size is smaller than the critical size, and then these fine spherical δ' precipitates will dissolve as the temperature increases. The volume fraction of θ' precipitates in 3# alloy is much greater than that in 2# alloy, while the volume fraction of T_1 precipitate is much lower than the latter. Only very limited T_1 precipitates formed along the dislocation are observed in the grain interior, indicating the increase of

Li concentration (from 1 wt% to 1.5 wt%) can promote the nucleation of θ' precipitates and simultaneously inhibit the formation of T_1 precipitates. In fact, it has been reported that the incubation time for T_1 precipitate nucleation in the Li-rich alloy (2196 alloy, with ~2 wt% Li) is much longer than that in the Li-poor alloy (2198 alloy, with ~1 wt% Li) [14]. The authors proposed that although the overall Li concentration of the Li-rich alloy is higher, the reduction of Li content in the matrix result from the precipitation of δ' phases in Li-rich alloy could provide a plausible explanation. Note that, the composition of 3# alloy in this work is similar to that of 2196 alloy, and the Li content of 2# alloy is slightly larger than that of 2198 alloy. Combining the TEM micrographs of two alloys in the as-quenched state, it can be inferred that the concentration of Li atoms available to form T_1 precipitates is low result from the formation of many δ' precipitates in 3# alloy, thereby suppressing the formation of T_1 precipitates. Moreover, the precipitation of θ' phase would be promoted due to the competitive precipitation relationship between θ' and T_1, which also provides a plausible explanation for the larger volume fraction of θ' precipitates in 3# alloy. Owing to the higher Li content and the lower Cu content, 6# alloy exhibits different microstructure characteristics. TEM micrographs of 6# alloy, as shown in Fig. 10e and f, reveal that only some β'/δ' precipitates and a large number of δ' precipitates exist in the grain interior. Compared with the as-quenched samples, typical δ' precipitates after aging are obviously less in number density and greater in diameter.

Fig. 11 displays TEM micrographs of the three alloys in UA state (32 h). The microstructure of 2# alloy is similar to the previous state, except for the growth of θ' and T_1 precipitates. It is worth mentioning that many T_1 precipitates are also observed in 3# alloy aged for 32 h, which may due to the gradual dissolution of δ' precipitate as the temperature increases, thus providing the necessary solute atoms for the nucleation and growth of T_1 precipitates. The volume fraction of δ'/θ'/δ' precipitate in 3# alloy decreases at the same time, which is owing to T_1 precipitate is considered to grow at the expense of θ' precipitate [32]. Note that, β' dispersoids with large size nucleated along the dislocation line are also observed, as shown in Fig. 11d. In terms of 6# alloy, apart from the growth of spherical δ' precipitate, a large number density of T_1 precipitates are also found near the grain boundary, as shown in Fig. 11e. However, there are hardly any θ' and T_1 precipitates in the grain interior.

Fig. 12 displays TEM micrographs of the three alloys in PA state. Based on the microhardness evolution (Fig. 8a), the time needed to obtain the peak-microhardness increases from 64 h for 2# and 3# alloys to 268 h for 6# alloy. As shown in Fig. 12a - d, the thickness of T_1 precipitate formed on the $\{111\}_{Al}$ plane in 2# and 3# alloys is extremely thin, and the appearance of T_1 precipitate presents no marked variation, except for the rapid growth of diameter. Besides, compared with the UA state, the diameter of θ' precipitates in the matrix significantly increases. Note that, in 2# and 3# alloys, the volume fraction of θ' precipitate is low in the T_1-rich area, and vice versa. It has been reported that T_1 precipitates would compete with θ' precipitates for available Cu atoms and heterogeneous nucleation sites in the α-Al matrix [33]. Moreover, no spherical δ' precipitate is observed in 2# and 3# alloys in PA state, indicating that the composition and heat treatment of the alloys cannot meet thermodynamic and kinetic requirements of the precipitation of spherical δ' phase. TEM micrographs of 6# alloy reveal that the spherical δ' precipitates in PA state are significantly less in number density and greater in diameter than those in UA state. Apart from β'/δ' and δ' precipitates, some T_1 and δ'/θ'/δ' plates are also observed. Generally, in cast Al-Li-Cu alloys, especially those with high lithium content, the nucleation of T_1 and θ' precipitates is much hard because of the extremely low density of dislocations, leading to a small amount of non-uniform distributed T_1 and θ' precipitates in the matrix [34].

Fig. 13 displays TEM micrographs of the three alloys in OA state. Fig. 13a and c are BF micrographs of 2# and 3# alloys in OA state, indicating the existence of numerous T_1 precipitates with immensely increased aspect ratio. Generally, T_1 precipitate is usually extremely

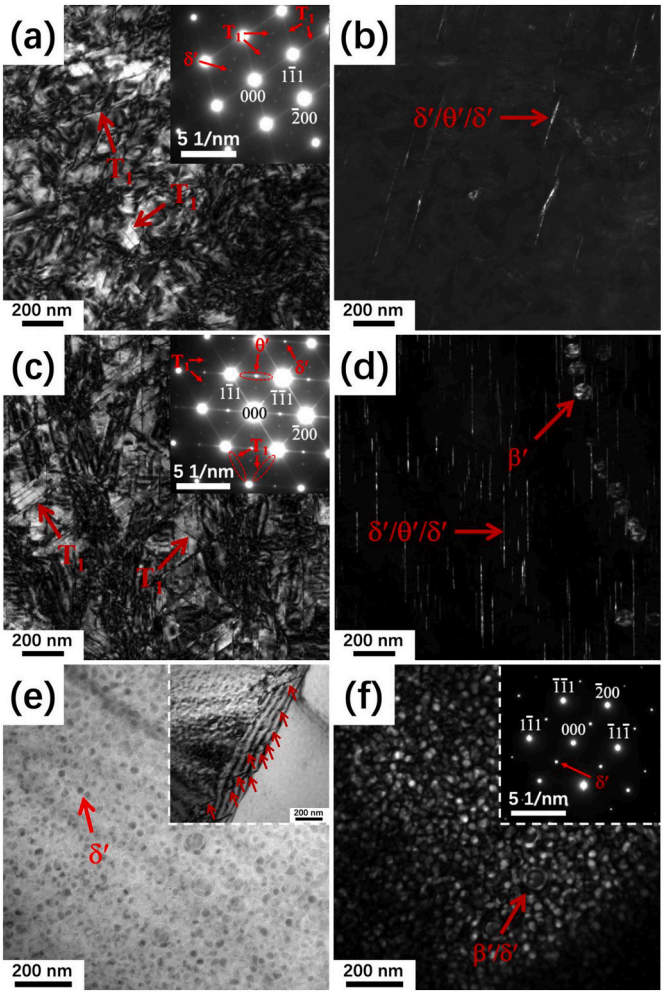

Fig. 11. TEM micrographs of the three alloys in UA state (32 h): (a) BF micrograph and SAD pattern viewed along $[011]_{Al}$ zone axis of 2# alloy; (b) the corresponding DF micrograph of 2# alloy; (c) BF micrograph and SAD pattern viewed along $[011]_{Al}$ zone axis of 3# alloy; (d) the corresponding DF micrograph of 3# alloy; (e) BF micrograph of grain interior and grain boundary of 6# alloy; (f) the corresponding DF micrograph and SAD pattern viewed along $[011]_{Al}$ zone axis of 6# alloy.

thin, ~1.3 nm in thickness, which is approximately five times the {111} spacing of Al, and it was recognized that the thickness of T_1 precipitate is very stable at ~170 °C [8]. Apart from the lengthening of T_1 precipitate, the coarsening of θ' precipitate is observed as well in both alloys, and its number density is lower than that in PA state, resulting in a decrease of the microhardness in OA state. Note that, the thickness of θ' precipitates in 2# and 3# alloys in OA state is much smaller than that in another conventional cast Al-4.5 wt% Cu alloy. Some authors suggested that the lenticular δ' precipitates nucleated heterogeneously on the two sides of θ' precipitate can inhibit the coarsening of θ' precipitate during isothermal aging and effectively ameliorate the microstructure stability [30]. In terms of 6# alloy, apart from the lengthening of T_1 precipitate and the coarsening of θ' precipitate, the size of spherical δ' precipitate increases significantly and it was reported that the coarsening of spherical δ' precipitate follows the L-S-W model, namely $r \propto t^{1/3}$ [35].

3.4. Mechanical properties

Table 3 lists the tensile test results, including ultimate tensile strength (UTS), yield strength (YS) and elongation (EL), of the alloys in different aging states. Typical engineering stress-strain curves of three alloys in different aging states are presented in Fig. 14. Exposure of the

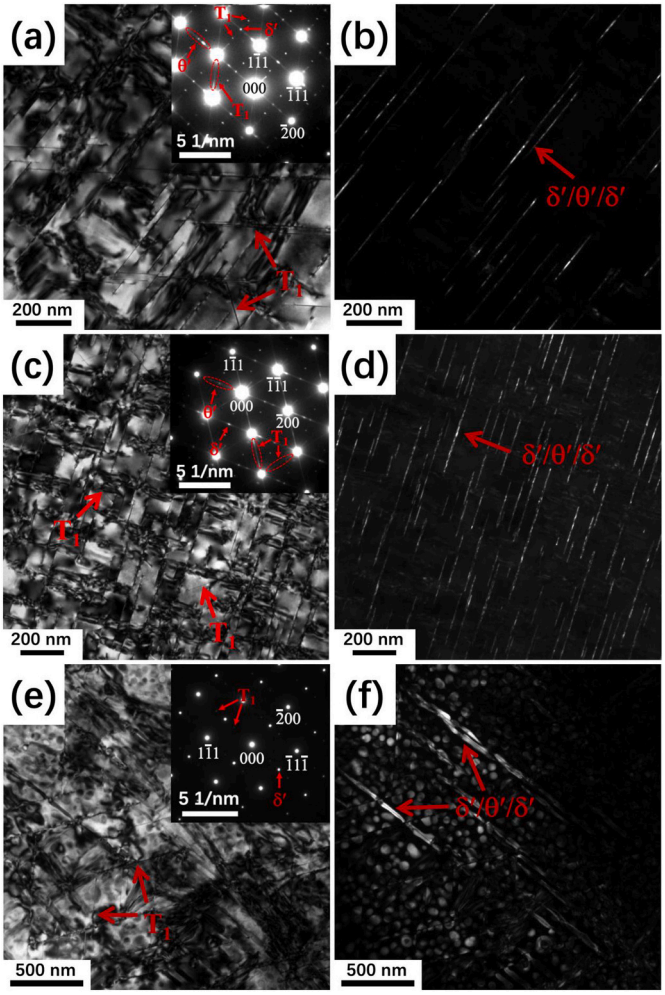

Fig. 12. TEM micrographs of the three alloys in PA state: (a) BF micrograph and SAD pattern viewed along $[011]_{Al}$ zone axis of 2# alloy; (b) the corresponding DF micrograph of 2# alloy; (c) BF micrograph and SAD pattern viewed along $[011]_{Al}$ zone axis of 3# alloy; (d) the corresponding DF micrograph of 3# alloy; (e) BF micrograph and SAD pattern viewed along $[011]_{Al}$ zone axis of 6# alloy; (f) the corresponding DF micrograph of 6# alloy.

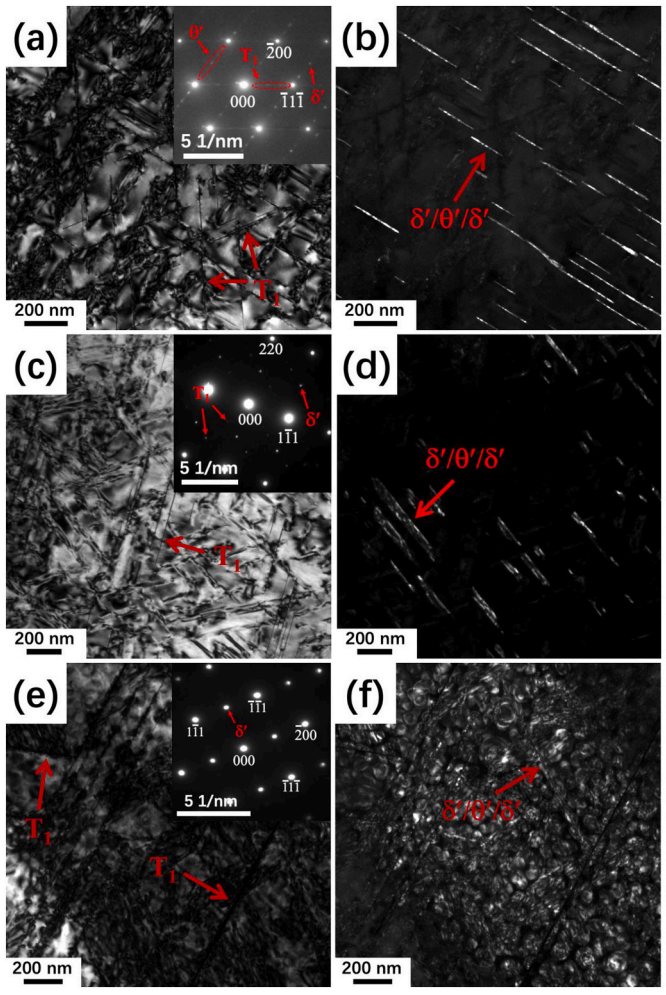

Fig. 13. TEM micrographs of the three alloys in OA state: (a) BF micrograph and SAD pattern viewed along $[011]_{Al}$ zone axis of 2# alloy; (b) the corresponding DF micrograph of 2# alloy; (c) BF micrograph and SAD pattern viewed along $[\bar{1}12]_{Al}$ zone axis of 3# alloy; (d) the corresponding DF micrograph of 3# alloy; (e) BF micrograph and SAD pattern viewed along $[011]_{Al}$ zone axis of 6# alloy; (f) the corresponding DF micrograph of 6# alloy.

alloys at 175 °C results in significant improvement of YS and UTS compared with those in as-quenched state, accompanied by different variations of EL. In terms of 2# alloy, UTS and YS greatly increase from 290 MPa and 112 MPa to 341 MPa and 208 MPa after 8 h, while its EL decreases from 23.1% to 12.9%. As aging, the strength of 2# alloy progressively increases concomitant with continuous decrease of ductility, and 3# alloy shows a similar trend. YS of 3# alloy markedly increases from 124 MPa after quenching to 221 MPa and 303 MPa for the samples aged for 4 and 16 h, respectively. As anticipated, EL decreases dramatically from 18.8% in the initial state to 5.6% for alloy aged for 4 h, and further decreases continuously with extending aging time. Note that, the results of 3# alloy aged for 32 h were not fully obtained as a result from its extremely limited ductility, which leads to premature fracture. In terms of 6# alloy, YS and UTS significantly increase from 123 and 306 MPa in as-quenched state to 277 and 367 MPa after 8 h, while its EL decreases sharply from 19.8% to 4.4%. Subsequently, YS increases slightly, accompanied by a further decrease of EL, which is consistent with its slow rate of microhardness increase during isothermal aging. However, its UTS is considered to remain stable within the error range. After 32 h, YS, UTS and EL of 6# alloy are 295 MPa, 366 MPa and 2.5%, respectively. According to TEM observation, the notable enhancement in strength of 6# alloy after aging is primally owing to the evolution of δ' precipitates, while of 2# and 3# alloys is mainly ascribed to T_1 and θ' precipitates. The best balance between strength (UTS = 414 MPa, YS = 350 MPa) and ductility (EL = 2.6%) is obtained by 2# alloy aged for 32 h. It is worth mentioning that 6# alloy has significant advantages in terms of density (2.437 g/cm^3) and elastic modulus (82.65 GPa) over 2# alloy (density: 2.675 g/cm^3; elastic modulus: 75.45 GPa).

Table 3
Mechanical properties of the alloys in different aging states.

Alloys	Aging state	Yield strength (MPa)	Ultimate tensile strength (MPa)	Elongation (%)
2#	175 °C - 8 h	208 ± 7	341 ± 6	12.9 ± 1.3
	175 °C - 32 h	350 ± 6	414 ± 9	2.6 ± 0.3
3#	175 °C - 4 h	221 ± 5	362 ± 7	5.6 ± 0.6
	175 °C - 16 h	303 ± 8	350 ± 9	1.4 ± 0.2
6#	175 °C - 8 h	277 ± 8	367 ± 5	4.4 ± 0.3
	175 °C - 32 h	295 ± 5	366 ± 5	2.5 ± 0.4

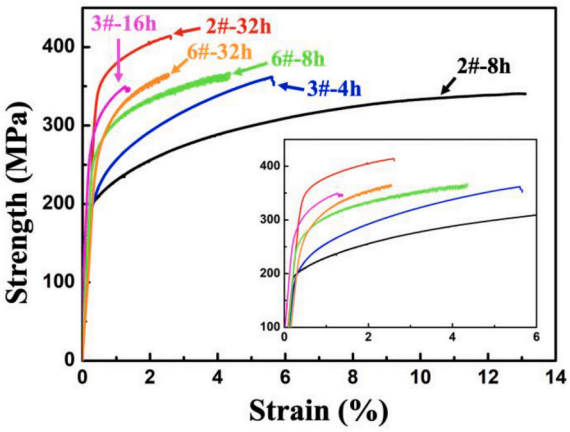

Fig. 14. Typical engineering stress-strain curves of the studied alloys in different aging states.

4. Conclusions

The effect of major constituents on microstructural evolution and mechanical properties of cast Al-Li-Cu-Zr alloy was studied. The principal findings are as follows:

1. The variations of the major constituents result in the changes of the type and volume fraction of the inter- and intra-granular intermetallic phases.
2. The solution parameters of the alloys are mainly determined by the Li content. The melting temperature progressively increases from 520 °C in 1# and 2# alloys to 560 °C in 6# alloy as the increase of Li content. Unfortunately, some insoluble intermetallic phases are observed in 4# alloy, hence the content of Li in cast Al-4.5 wt% Cu alloy should not exceed 1.5 wt%.
3. All alloys possess a strong aging-hardening, and the microhardness increments of the three alloys during isothermal aging are approximately the same. The time required to obtain the peak-microhardness increases from 64 h for 2# and 3# alloys to 268 h for 6# alloy. The highest peak-microhardness is obtained in 3# alloy (176.4 HV), followed by 6# alloy and 2# alloy.
4. The contents of the major constituents significantly affect the precipitation behavior, including the kinetics and sequence of precipitation, during isothermal aging. The Li-poor alloy (2# alloy) presents a much shorter incubation time of T_1 precipitate than the Li-rich alloy (3# alloy), while the nucleation of θ' precipitate is promoted in Li-rich alloy. No typical spherical δ' precipitate is observed in 2# and 3# alloys, except for the as-quenched 3# alloy. δ' precipitate preferentially nucleates on the broad and coherent face of θ' precipitate in 2# and 3# alloys, resulting in the formation of "sandwich-like" δ'/θ'/δ' precipitates. Further decreasing Cu content to 2 wt% and increasing Li content to 3 wt%, the predominant phase in the matrix is spherical δ' precipitate, accompanied by a small amount of unevenly distributed T_1 and θ' precipitates.
5. The best balance between strength (UTS = 414 MPa, YS = 350 MPa) and ductility (EL = 2.6%) is obtained by 2# alloy aged at 175 °C for 32 h. However, 6# alloy has significant advantages in terms of density (2.437 g/cm^3) and elastic modulus (82.65 GPa) over 2# alloy (density: 2.675 g/cm^3; elastic modulus: 75.45 GPa). According to TEM observation, it can be concluded that the notable enhancement in strength of 6# alloy after aging is primally owing to the evolution of δ' precipitates, while of 2# and 3# alloys is mainly ascribed to T_1 and θ' precipitates.

Data availability

The raw/processed data required to reproduce these findings cannot be shared at this time as the data also forms part of an ongoing study.

Declaration of Competing Interest

The authors declare that they have no known competing financial interests or personal relationships that could have appeared to influence the work reported in this paper.

Acknowledgments

L. Wu is grateful for the scholarship supported by the China Scholarship Council (Grant no. 201906230200). The authors would like to thank Dr. Sungil Baik and Dr. Fei Xue at Northwestern University for their assistance.

References

[1] J.C. Williams, E.A. Starke Jr., Progress in structural materials for aerospace systems, Acta Mater. 51 (2003) 5775–5799.
[2] A. Deschamps, C. Sigli, T. Mourey, F. De Geuser, W. Lefebvre, B. Davo, Experimental and modelling assessment of precipitation kinetics in an Al–Li–Mg alloy, Acta Mater. 60 (2012) 1917–1928.
[3] S.J. Kang, T.-H. Kim, C.-W. Yang, J.I. Lee, E.S. Park, T.W. Noh, M. Kim, Atomic structure and growth mechanism of T_1 precipitate in Al–Cu–Li–Mg–Ag alloy, Scr. Mater. 109 (2015) 68–71.
[4] E. Lavernia, T.S. Srivatsan, F. Mohamed, Strength, deformation, fracture behaviour and ductility of aluminium-lithium alloys, J. Mater. Sci. 25 (1990) 1137–1158.
[5] V. Araullo-Peters, B. Gault, F. De Geuser, A. Deschamps, J.M. Cairney, Microstructural evolution during ageing of Al–Cu–Li–x alloys, Acta Mater. 66 (2014) 199–208.
[6] L. Wu, X. Li, G. Han, Y. Deng, N. Ma, H. Wang, Precipitation behavior of the high-Li-content in-situ TiB_2/Al-Li-Cu composite, Mater. Charact. 132 (2017) 215–222.
[7] B. Gault, X.Y. Cui, M.P. Moody, F. De Geuser, C. Sigli, S.P. Ringer, A. Deschamps, Atom probe microscopy investigation of Mg site occupancy within δ' precipitates in an Al–Mg–Li alloy, Scr. Mater. 66 (2012) 903–906.
[8] A. Deschamps, B. Decreus, F. De Geuser, T. Dorin, M. Weyland, The influence of precipitation on plastic deformation of Al–Cu–Li alloys, Acta Mater. 61 (2013) 4010–4021.
[9] B. Gable, A. Zhu, A. Csontos, E. Starke Jr., The role of plastic deformation on the competitive microstructural evolution and mechanical properties of a novel Al–Li–Cu–X alloy, J. Light. Met. 1 (2001) 1–14.
[10] R. Yoshimura, T.J. Konno, E. Abe, K. Hiraga, Transmission electron microscopy study of the early stage of precipitates in aged Al–Li–Cu alloys, Acta Mater. 51 (2003) 2891–2903.
[11] R. Yoshimura, T.J. Konno, E. Abe, K. Hiraga, Transmission electron microscopy study of the evolution of precipitates in aged Al–Li–Cu alloys: the θ' and T_1 phases, Acta Mater. 51 (2003) 4251–4266.
[12] P. Donnadieu, Y. Shao, F. De Geuser, G. Botton, S. Lazar, M. Cheynet, M. De Boissieu, A. Deschamps, Atomic structure of T_1 precipitates in Al–Li–Cu alloys revisited with HAADF-STEM imaging and small-angle X-ray scattering, Acta Mater. 59 (2011) 462–472.
[13] S. Wang, M. Starink, Precipitates and intermetallic phases in precipitation hardening Al–Cu–Mg–(Li) based alloys, Int. Mater. Rev. 50 (2005) 193–215.
[14] B. Decreus, A. Deschamps, F. De Geuser, P. Donnadieu, C. Sigli, M. Weyland, The influence of Cu/Li ratio on precipitation in Al–Cu–Li–x alloys, Acta Mater. 61 (2013) 2207–2218.
[15] R.J. Rioja, J. Liu, The evolution of Al-Li base products for aerospace and space applications, Metall. Mater. Trans. A 43 (2012) 3325–3337.
[16] E. Gumbmann, F. De Geuser, C. Sigli, A. Deschamps, Influence of Mg, Ag and Zn minor solute additions on the precipitation kinetics and strengthening of an Al-Cu-Li alloy, Acta Mater. 133 (2017) 172–185.
[17] L. Wu, C. Zhou, X. Li, N. Ma, H. Wang, Microstructural evolution and mechanical properties of cast high-Li-content TiB_2/Al-Li-Cu composite during heat treatment, J. Alloys Compd. 739 (2018) 270–279.
[18] D. Tsivoulas, J. Robson, Heterogeneous Zr solute segregation and Al_3Zr dispersoid distributions in Al–Cu–Li alloys, Acta Mater. 93 (2015) 73–86.
[19] K. Baveja, Dynamic method of measuring Young's modulus of elasticity, J. Sci. Instrum. 41 (1964) 662–665.
[20] K. Hono, S. Babu, K. Hiraga, R. Okano, T. Sakurai, Atom probe study of early stage phase decomposition in an Al-7.8 at.% Li alloy, Acta Metall. Mater. 40 (1992) 3027–3034.
[21] L. Wu, C. Zhou, X. Li, N. Ma, H. Wang, Effects of TiB_2 particles on artificial aging response of high-Li-content TiB_2/Al-Li-Cu composite, J. Alloys Compd. 749 (2018) 189–196.
[22] F. Wang, Z. Liu, D. Qiu, J.A. Taylor, M.A. Easton, M.-X. Zhang, Revisiting the role of peritectics in grain refinement of Al alloys, Acta Mater. 61 (2013) 360–370.

[23] Y. Du, Y. Chang, B. Huang, W. Gong, Z. Jin, H. Xu, Z. Yuan, Y. Liu, Y. He, F.-Y. Xie, Diffusion coefficients of some solutes in fcc and liquid Al: critical evaluation and correlation, Mater. Sci. Eng. A 363 (2003) 140–151.
[24] A. Chen, G. Wu, L. Zhang, X. Zhang, C. Shi, Y. Li, Microstructural characteristics and mechanical properties of cast Al-3Li-xCu-0.2Zr alloy, Mater. Sci. Eng. A 677 (2016) 29–40.
[25] K. Kumar, F. Heubaum, The effect of Li content on the natural aging response of Al-Cu-Li-Mg-Ag-Zr alloys, Acta Mater. 45 (1997) 2317–2327.
[26] V. Radmilovic, A. Fox, G. Thomas, Spinodal decomposition of Al-rich Al-Li alloys, Acta Metall. 37 (1989) 2385–2394.
[27] F.W. Gayle, J.B. Vander Sande, "Composite" precipitates in an Al-Li-Zr alloy, Scr. Metall. 18 (1984) 473–478.
[28] H. Flower, P. Gregson, Solid state phase transformations in aluminium alloys containing lithium, Mater. Sci. Technol. 3 (1987) 81–90.
[29] L. Wu, Y. Li, X. Li, N. Ma, H. Wang, Interactions between cadmium and multiple precipitates in an Al-Li-Cu alloy: Improving aging kinetics and precipitation hardening, J. Mater. Sci. Technol. 46 (2020) 44–49.
[30] S. Duan, C. Wu, Z. Gao, L. Cha, T. Fan, J. Chen, Interfacial structure evolution of the growing composite precipitates in Al-Cu-Li alloys, Acta Mater. 129 (2017) 352–360.
[31] C. Yang, P. Zhang, D. Shao, R. Wang, L. Cao, J. Zhang, G. Liu, B. Chen, J. Sun, The influence of Sc solute partitioning on the microalloying effect and mechanical properties of Al-Cu alloys with minor Sc addition, Acta Mater. 119 (2016) 68–79.
[32] M. Tosten, A. Vasudevan, P. Howell, The aging characteristics of an AI-2 Pct Li-3 Pct Cu-0.12 Pct Zr alloy at 190° C, Metall. Trans. A. 19 (1988) 51–66.
[33] J. Kim, J.K. Park, Effect of stretching on the precipitation kinetics of an Al-2.0 Li-2.8 Cu-0.5 Mg (−0.13 Zr) alloy, Metall. Mater. Trans. A 24 (1993) 2613–2621.
[34] W. Cassada, G. Shiflet, E. Starke, The effect of plastic deformation on Al_2CuLi (T_1) precipitation, Metall. Trans. A. 22 (1991) 299–306.
[35] B. Pletcher, K. Wang, M. Glicksman, Experimental, computational and theoretical studies of δ' phase coarsening in Al–Li alloys, Acta Mater. 60 (2012) 5803–5817.